Effective permittivity of compacted granular materials: Effects of interfacial polarization and pore-filling fluids

Xu Wang [a], Chongpu Zhai [b,*], Yixiang Gan [a,c,*]

[a] *School of Civil Engineering, The University of Sydney, Sydney NSW 2006, Australia*
[b] *State Key Laboratory for Strength and Vibration of Mechanical Structures, School of Aerospace Engineering, Xi'an Jiaotong University, Xi'an 710049, China*
[c] *The University of Sydney Nano Institute (Sydney Nano), The University of Sydney, Sydney NSW 2006, Australia*

ARTICLE INFO

ABSTRACT

Interfacial polarization dominates the permittivity spectra of heterogeneous granular materials for the intermediate frequency range (*i.e.*, from kHz to MHz). In this study, we examine the corresponding dielectric responses of compacted glass sphere packings saturated with pore-filling fluids under various compressive stresses. The effective permittivity spectra are observed to exhibit consistently a plateau-to-plateau drop, described by low-frequency permittivity, characteristic frequency, and high-frequency permittivity. The permittivity spectra under different compressive levels are found to be influenced by the packing structure, compressive stress, and electrical property contrasts between solid and fluid (specifically permittivity and conductivity). For considered measurement conditions, the variation of packing structure and its associated porosity is found to be more significant than the stress evolution in controlling the interfacial polarization, thus the permittivity spectra, as supported by analytical and numerical results for unit cells. Furthermore, to gain a general rule for dielectric responses for saturated granular materials, we train multi-layer artificial neural network (ANN) models based on a series of simulations for unit cells with various structures, stresses, and electrical and dielectric properties. The predictions with two-layer ANN agree well with experimental measurements, presenting errors smaller than 5% for both low-frequency and high-frequency permittivity. This study offers an effective predicting approach for the dielectric behaviour of heterogeneous and multiphase materials.

1. Introduction. The permittivity of granular materials is of immense significance in many technological and industrial applications, such as novel dielectric materials [1], sensing and detection devices [2,3], and energy storage and transmission equipment [4]. Multiple phases heterogeneous mixtures often employed in these applications, including multilayer-structure dielectrics [5], ceramic filler and polymer matrix of nanocomposite material [6,7], blood cell suspensions [8], and saturated granular materials [9–11]. At intermediate frequencies (*i.e.*, from kHz to MHz), it is well accepted that interfacial polarization [11], which occurs at the interfaces between phases with contrasting electrical properties, will dominate the effective permittivity of the heterogeneous materials. On the microscopic scale, within a heterogeneous material characterized by spatial variations in electrical conductivity σ and permittivity ε, the charge density in the limit of direct current is $\rho = \sigma(\nabla \frac{\varepsilon}{\sigma} \cdot E)$. This disparity of charge distribution emerges at the interfaces where an abrupt change in the gradient of ε/σ presents. The discontinuity in electrical properties prompts the accumulation of positive and negative charges separated by the interfaces; thereby, the interfaces are polarized, resulting in additional energy storage in response to the external electric field [12–15]. Consequently, the effects of interfacial polarization accumulate throughout the system, thus leading to the variation of the effective permittivity over a certain range of frequencies. When external compression is introduced to the multi-phased granular materials, the complexity of depicting the effective permittivity increases due to the occurring variations of local pore structure [16–18], contact force network [19–21], and interactions at solid-liquid interfaces [11,22], However, these factors have been paid less attention, or partially neglected.

For simplification, existing studies taking account of interfacial polarization effects often use dipolar approximation where multipole interaction due to the complexity of granular structure is neglected in analysing the effective permittivity of saturated granular materials [14,23,24]. Structure evolutions under compressive loads, such as the particle rearrangement and renewing of inter-particle contact, are typically summarised by a single structure parameter, *i.e.*, the varying porosity [15,25-27]. The estimated permittivity spectra demonstrate apparent differences in terms of the characteristic frequency and plateau per-

---

* Corresponding authors.
E-mail addresses: zhaichongpu@xjtu.edu.cn (C. Zhai), yixiang.gan@sydney.edu.au (Y. Gan).

mittivity at low and high frequencies. Moreover, the measurement of effective permittivity in porous media provides a practical method of determining porosity and saturation levels of granular materials [28]. This approach is particularly valuable when there are substantial contrasts in the electrical properties between the solid phase and the pore fluid [23,29]. Empirical equations have been developed to link effective permittivity to saturation levels [30–32], emphasizing the dominant role of the pore fluid permittivity. However, these empirical solutions typically only function well over frequencies in the microwave region [31]. For lower frequencies *i.e.*, an intermediate range from kHz to MHz, where interfacial polarization at solid-liquid interfaces matters, the frequency-dependent effective permittivity could not be accurately interpreted, showing disparities with respect to experimental observations [33]. Therefore, packing structures, stress levels, microstructure deformations, and electrical properties of involved solids and pore fluids are all essential to gain a comprehensive understanding of dielectric responses of heterogeneous multiphase granular materials.

Studies of permittivity in heterogeneous material have been advanced in conjunction with the development of the effective medium theory (EMT), which is a theoretical modelling approach employed to predict the effective properties of a composite medium, given the properties of its individual constituents and their respective volume fractions. Maxwell Garnett [34] and Bruggeman [35] introduced the theoretical framework for dilute low-contrast interchangeable spherical dispersions. Followed by Hashin and Shtrikman [36], the upper and lower bounds for the effective properties of two-phase materials were established. Maxwell [12] first highlighted the concept of dielectric dispersion due to interfacial polarization through a stratified model. Wagner [26] proposed one of the earliest models developed to address the interfacial polarization effects of the effective permittivity of heterogenous materials, where spherical grains are sparsely distributed in a host medium. The effective complex permittivity $\varepsilon_{\text{eff}}^*$ of the composite is expressed as:

$$\frac{\varepsilon_{\text{eff}}^* - \varepsilon_{\text{p}}^*}{\varepsilon_{\text{eff}}^* + 2\varepsilon_{\text{p}}^*} = \varphi_{\text{s}} \frac{\varepsilon_{\text{s}}^* - \varepsilon_{\text{p}}^*}{\varepsilon_{\text{s}}^* + 2\varepsilon_{\text{p}}^*}, \tag{1}$$

where φ_{s} is the volume fraction of the solid phase and ε_{s}^* and ε_{p}^* are the complex permittivity of solid and pore phases, respectively. However, these early works primarily apply to dilute concentrations within nonconductive host media [15]. Subsequently, the differential effective medium theory (DEMT) emerged, combining EMT and Wagner's homogenization. DEMT constructs a composite by introducing infinitesimal spherical inclusions into a homogeneous medium through iterative Wagner's homogenization processes until the desired porosity is achieved [14]. In DEMT modelling, the shape, distribution and orientation of grains can be modified to a certain extent by altering the infinitesimal elements replaced in the homogenization process, allowing for consideration of material texture [37–40]. The effective complex permittivity $\varepsilon_{\text{eff}}^*$ with spherical grains can be expressed as

$$1 - \varphi_{\text{s}} = \frac{\varepsilon_{\text{eff}}^* - \varepsilon_{\text{s}}^*}{\varepsilon_{\text{p}}^* - \varepsilon_{\text{s}}^*} \left(\frac{\varepsilon_{\text{p}}^*}{\varepsilon_{\text{eff}}^*} \right)^{1/3}. \tag{2}$$

Notably, DEMT primarily finds its applicability in colloidal suspensions characterized by high porosity values, which employs the multiple scattering techniques and the single matrix approximation, focusing on the homogeneous equivalent medium while neglecting electrical interactions between neighbouring grains [24,41]. Consequently, a gap in the literature remains where no model has been demonstrated to effectively account for strongly heterogeneous granular materials with porosities below 0.5 [39]. Furthermore, scant attention has been devoted to the exploration of the influence of both grain-level electrical and mechanical interactions on interfacial polarization effects [42]. This aspect becomes particularly pertinent when considering geological samples situated deep within the subsurface, exposed to substantial earth pressures, rendering the comprehension of interfacial polarization effects

on deformed structures a challenging endeavour. Regrettably, limited research has been dedicated to this specific domain. Additionally, it is noteworthy that existing literature often assumes only one of the phases is conductive [24,38,43]. A comprehensive examination of the impact of conductivity and permittivity contrasts between the solid and pore fluid on effective permittivity variation due to interfacial polarization is absent.

Advances in computational techniques have brought the integration of numerical simulations, such as the finite difference time domain method, finite element analysis (FEA), and pore-scale simulations, as potent tools for investigating the electrostatic responses of heterogeneous structures [24,44-46]. These simulations have been crucial in extending our understanding beyond the confines of EMT models. Researchers have delved into various factors, including inclusion size distributions [47–49], complex geometries [43,44,50], packing arrangements of inclusions [51–53], surface coatings [54,55], etc. These investigations have progressively refined our understanding of the effective permittivity of complex materials. In FEA simulations, the effective permittivity of samples is calculated by directly solving the Maxwell equation within a unit cell, and the packing states and microstructure can be characterized [8]. This approach provides a robust framework for studying the effects of packing arrangements and microstructural deformations on the effective properties of heterogeneous multiphase granular materials. Additionally, many emerging applications in material science using machine learning and artificial neural networks (ANNs) involve supervised learning [56,57], where the models are trained by given input features and target outputs. Once adequately trained, these models can predict target values based solely on input features. Lately, many studies have unravelled the hidden details of transport through complex networks in porous and granular materials with the help of ANN, including interfacial thermal resistance [58,59], permeability [57] and electrochemical ion and electrolyte transport [60,61]. Therefore, ANN shows its potential in dealing with complexity brought by the heterogeneous microstructural characteristics, material and mechanical properties.

In this paper, we first demonstrate our experimental setup, the numerical modelling processes, and the ANN training approach for evaluating the effective permittivity over the frequency range, dominated by the mechanism of interfacial polarization, for the compacted granular materials saturated with pore-filling fluid. Then, we present the comparison results on effective permittivity characteristics due to interfacial polarization obtained from experimental measurements and numerical simulations focusing on the effects of packing arrangement, stress state, microstructure deformation, and electrical property contrasts. Finally, metamodels are trained by simulation results and used to predict the experimentally observed effective permittivity characteristics.

2. Methods.

2.1. Experimental section. Monosized spherical glass particles (SiO_2) with a diameter of 4 mm are randomly packed in a nonconductive waterproofed cylinder (Al_2O_3), as shown in the schematic in Fig. 1(a). The cylinder has dimensions of 95 mm in height (H) and 100 mm in diameter (D), topped and bottomed by two circular stainless-steel plates (AISI 304, grade G200) as electrodes. Subsequently, the packed glass beads are filled with deionized water (Lab grade $\sigma < 5 \times 10^{-4}$ s/m). The complex impedance Z ($Z = Z' + Z''j$, where Z' and Z'' are real and imaginary parts of the impedance) is measured by Agilent 4294A, over the frequency range from 1 kHz to 1 MHz. In our experiments, three random packings with initial porosity of 0.349, 0.369 and 0.379 are considered and impedance analyses are carried out at varying compression from 13.93 kPa to 255.85 kPa. Before each measurement, both electrodes are thoroughly cleaned using detergent and deionized water to ensure the measurement quality. Additionally, the sinusoidal wave with an amplitude of 100 mV is employed, minimizing the electrolytic process at the liquid-electrode interfaces. The total capacitance, C_{exp}, of the saturated packing is derived based on the measured complex impedance, $C_{\text{exp}} = \frac{\text{imag}(1/Z)}{2\pi f}$. Then, the modified parallel capacitor equation is ap-
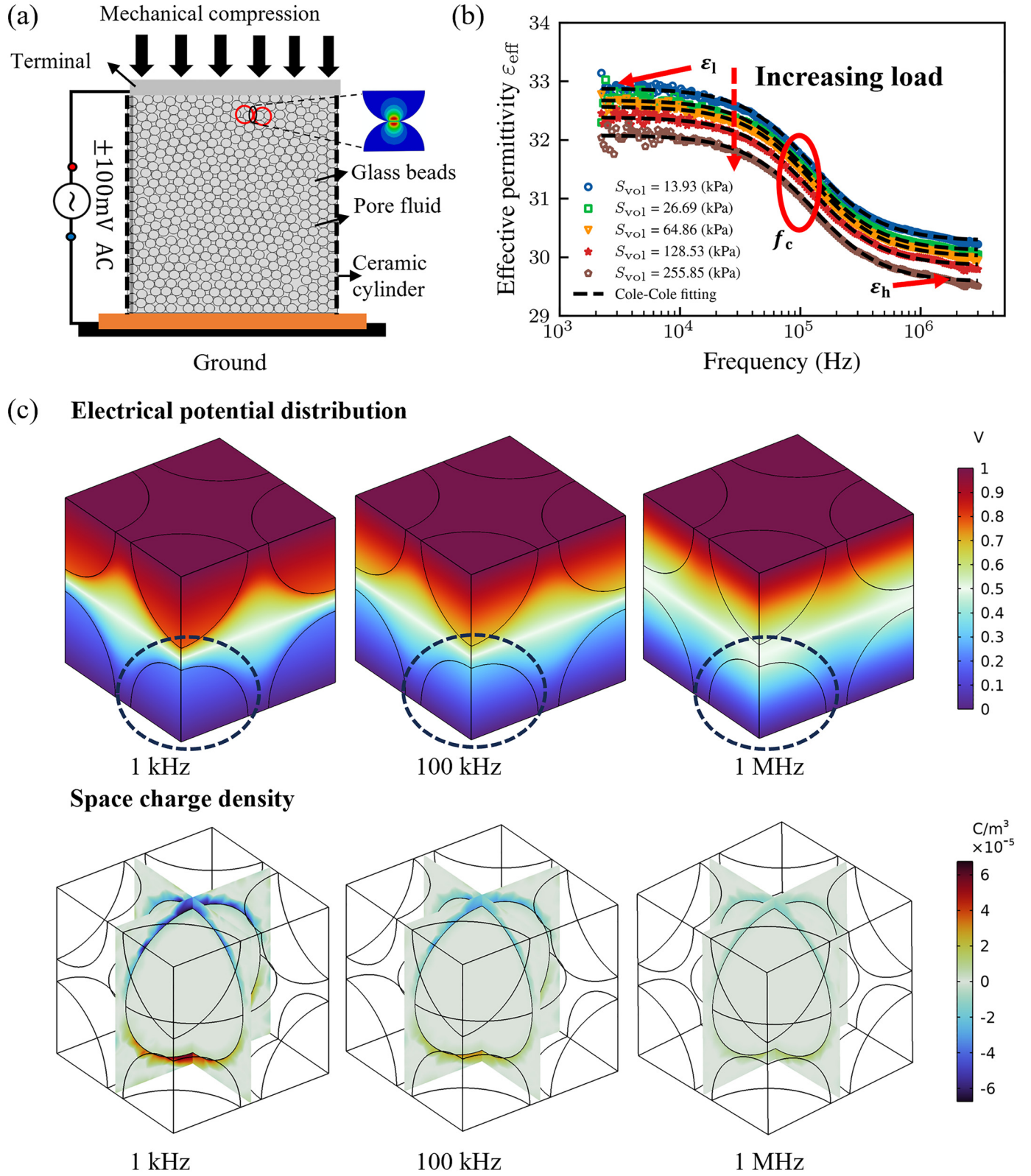
Fig. 1. (a) Schematic of impedance measurements for saturated granular materials under compression. (b) Experimental observations of dielectric spectra under increasing normal compression for a typical case with initial porosity $\varphi = 0.349$. The interfacial polarization induced low-frequency ε_l, characteristic frequency f_c and high-frequency permittivity ε_h are shown, which are determined by Cole-Cole model fitting (as dashed lines). (c) FEA results of the distributions of electric potential (top) and space charge (bottom) for an uncompressed body-centered cubic (BCC) unit cell at different frequencies.

Table 1

Fitting parameters of the Cole-Cole model for experimental case with $\varphi = 0.349$.

Compression stress (kPa)	$\Delta\varepsilon_{\text{eff}}$	f_c (kHz)	ε_{h}
13.93	32.88	119.25	30.28
26.69	32.68	119.63	30.10
64.86	32.57	121.92	30.01
128.53	32.39	121.72	29.85
255.85	32.08	122.65	29.58

plied to calculate the relative effective permittivity,

$$\varepsilon_{\text{eff}} = \frac{4(H - \Delta H)}{\varepsilon_0 \pi D^2} \left(C_{\exp} - C_{\text{corr}} \right), \tag{3}$$

where ε_0 is the permittivity of vacuum (8.854×10^{-12} F/m), and C_{corr} is the capacitance correction to exclude potential electrode polarization effects between the electrode and the tested sample [62]. Due to the nondimensional quantity used above, the permittivity terms reported in this study contain no physical unit. The obtained ε_{eff} spectra under increasing normal compression are provided in Fig. 1(b). For all loading levels, ε_{eff} plateaus can be observed when the frequency is below 10 kHz, followed by a gradual decrease. The decrease rate reaches the peak at the characteristic frequency f_c.

Given the discrete nature of the effective permittivity measured in the frequency domain, the Cole-Cole relaxation model is employed to fit the discrete data and to extract the onset of ε_{eff} drop, high-frequency permittivity ε_l and characteristic frequency f_c [15]:

$$\varepsilon_{\text{eff}} = \varepsilon_{\text{h}} + \frac{\varepsilon_l - \varepsilon_{\text{h}}}{1 + (\omega\tau)^{1-\alpha}}, \tau = \left(2\pi f_c\right)^{-1}, \tag{4}$$

where ε_l and ε_{h} represents the interfacial polarization induced low-frequency and high-frequency permittivity plateau, respectively. τ is the relaxation time, which is the reciprocal of the characteristic frequency f_c. The relaxation time τ signifies the timescale at which the interfacial polarization response occurs. The exponent parameter α takes a value between 0 and 1, allowing the description of different spectral shapes. It is consistently set at 0.25 for all experimental cases. The experimental measurements and fitted Cole-Cole models are provided in Fig. 1(b), demonstrating negligible errors (less than 0.05%). The effective permittivity plateaus (ε_l, ε_{h}) and characteristic frequency f_c at various compressive stresses for experiment cases with initial porosity of 0.349 are provided in Table 1. For the considered loading levels, ε_l continuously decreases from 32.88 to approximately 32.08 as the compression increases from 13.93 kPa to 255.85 kPa, indicating that external compressions reduce the effects of interfacial polarization in the test sample. In contrast, the characteristic frequency f_c exhibits an opposite trend, increasing from approximately 119.25 kHz to 122.65 kHz as fewer charges are involved in the interfacial polarization process [63].

2.2. Unit cell models. To further reveal the underlying mechanism governing the dielectric responses in water-saturated granular packing of monosized glass spheres, numerical simulations were employed on three periodically structured unit cells (simple cubic, body-centred cubic, and face-centred cubic) for various packing arrangements, volumetric compression, conductivity and permittivity contrasts between solid and pore fluid. These unit cells served as representative elementary volumes for their respective regular packings, exhibiting distinguished porosities and coordination numbers. For considered unit cells, the coordination number, calculated by $CN = 2\frac{N_{\text{contact}}}{N_{\text{particle}}}$ and porosity φ, given as $\varphi = \frac{v_{\text{p}}}{v_{\text{t}}}$, increase from 6 (SC) to 12 (FCC) and from 0.26 (FCC) to 0.477 (SC), respectively. It is important to highlight that the initial porosity of the random packing used in experiments is approximately 0.372.

To demonstrate the simulation procedure, we initially conducted the simulation of the compaction process for the unit cells under increasing volumetric stress. Here, the pore water is excluded since reaction forces were primarily facilitated by contact forces between solid particles, and

the variation of inter-particle force and the induced deformation are computed based on the hard contact model [64]. We subsequently import the deformed geometries into COMSOL Multiphysics, with the electrical properties of glass and water being assigned to the solid and pore spaces, respectively. An electrical potential difference of 1 V is applied to opposite sides of the unit cell as positive electrode and ground. Furthermore, we perform electric current simulations for discrete frequencies to replicate the frequency-dependent impedance variations within these unit cells. Ultimately, the effective permittivity is computed based on impedance data obtained from these simulations. This comprehensive workflow enables us to simulate the effects of mechanical deformation in granular systems, thereby advancing our understanding of the intricate relationship between microstructure deformations and dielectric responses due to interfacial polarization.

2.3. Artificial neural network (ANN). A multi-layer ANN comprises one input layer, one or more hidden layers, and an output layer; neurons in a given layer are fully connected to those in the subsequent layer. The training process involves feeding the training dataset into the hidden layers for model training. Subsequently, the model is assessed by validation data to fine-tune model hyperparameters. At last, the model performance is evaluated using the test dataset. The weight values of each input feature are updated through the backpropagation training algorithm. For each training data, the output of each neuron is calculated by the training algorithm, and the results are fed forward to the output layer. Then, MSE is used to determine the error each neuron contributes to, which is backpropagated to the input layer, and the corresponding weights are updated based on gradient descent. In current work, the hyperbolic tangent activation functions are used in all neural networks.

In this study, we integrate modern advances in numerical modelling and statistics (ANN) to develop a data-driven framework tailored for multiscale and nonlinear transport phenomena in granular systems. Our approach distinguishes itself from past efforts [15,24,33] in two aspects. First, our investigation delves into the critical factors exerting substantial influences on dielectric responses of saturated granular material across the kHz to MHz frequency range. These factors encompass packing configurations, microstructure deformations, and electrical property contrasts, which are studied through a combination of experimental and numerical methods and then compared with theoretical models to assess their applicability in low-porosity heterogeneous systems. Second, we fuse numerical simulations with an artificial neural network to establish a data-driven metamodel. This metamodel enables incorporating the aforementioned factors as input features, facilitating the prediction of effective permittivity characteristics arising from interfacial polarization. This synergistic approach enhances our understanding of complex granular systems and provides a robust predictive tool for their dielectric behaviours.

3. Results and discussion.

3.1. Effective permittivity variation dominated by interfacial polarization. In general, the effective permittivity ε_{eff} experiences a decrease with frequency for the glass sphere packing saturated with deionized water under all levels of compression in the experiments. For example, the ε_{eff} of the sample subjected to 13.93 kPa compressive stress decreases from approximately 32.88 at 1 kHz to approximately 30.08 at 1 MHz as shown in Fig. 1(b). These observed enhanced polarizability at lower frequencies is attributed to the buildup charges due to the electrical property discrepancies between glass and deionized water, occurring at the solid-water interfaces of the experiment sample. As frequency increases, there is less time available for charges to accumulate at the interfaces due to the rapidly changing electric field direction, leading to a diminished interfacial polarization effect at higher frequencies. These charge accumulations at phase boundaries at low frequencies can also be observed in FEA simulations. This shifts the electric field distribution due to the charge buildup until a state of equilibrium is reached in terms of current density within the two phases [45]. As frequency increases, interfacial polarization diminishes, and the electric field distribution changes dra-
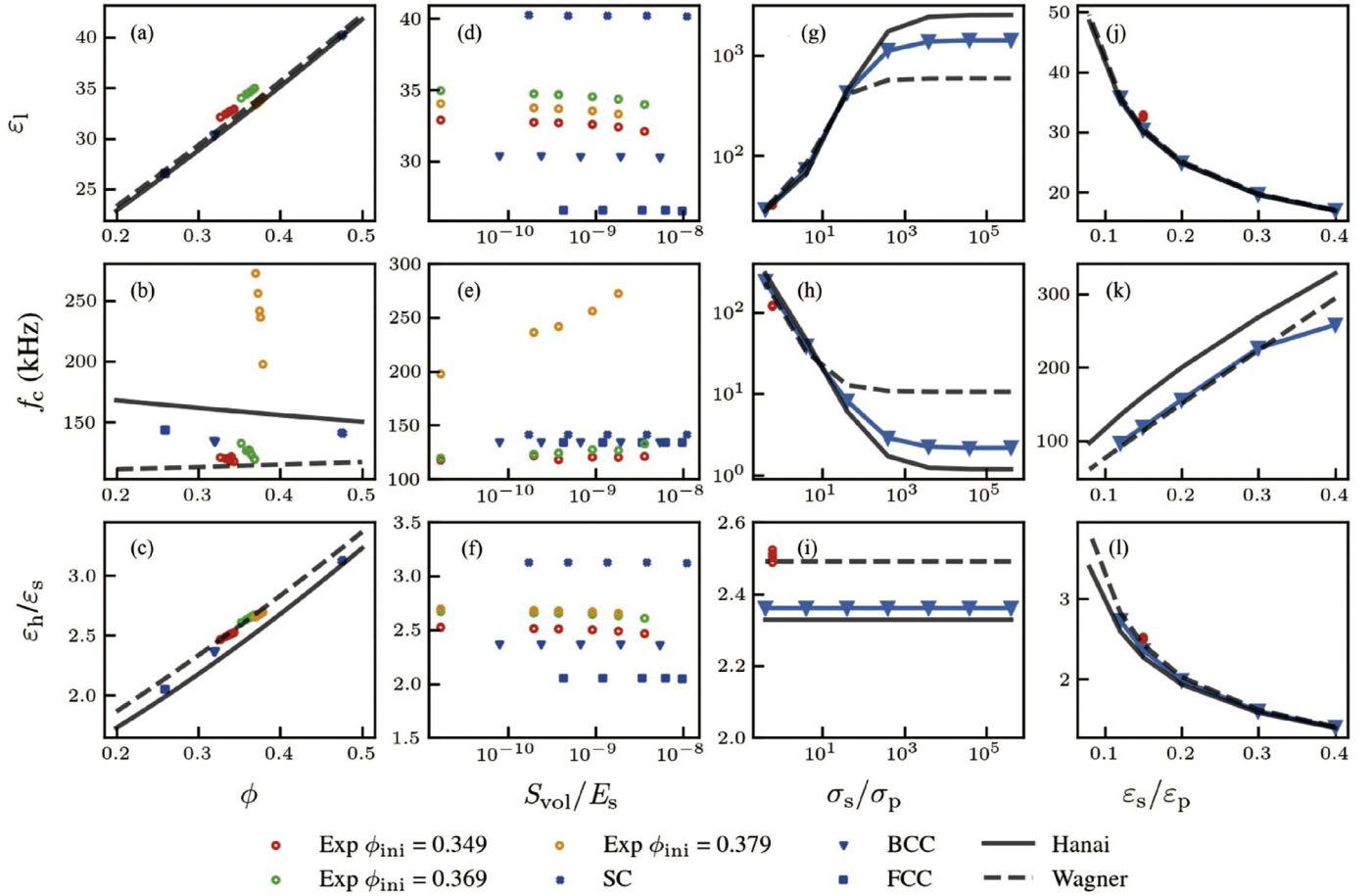
Fig. 2. Effects of porosity φ, normalized compressive stress $S_{\mathrm{vol}}/E_{\mathrm{s}}$, electrical conductivity contrast $\sigma_{\mathrm{s}}/\sigma_{\mathrm{p}}$ and permittivity contrast $\varepsilon_{\mathrm{s}}/\varepsilon_{\mathrm{p}}$ (Column 1–4) on low-frequency effective permittivity ε_{l}, characteristic frequency f_{c} and normalized high-frequency effective permittivity $\varepsilon_{\mathrm{h}}/\varepsilon_{\mathrm{s}}$ (Row 1–3): comparison among experiment measurements (hollow circles with different colours stand for different initial porosity), FEA unit cells (cross for SC, triangles for body-centered cubic (BCC), and squares for FCC), and theoretical models (solid and dash lines). For the effect of porosity on normalized high-frequency permittivity $\varepsilon_{\mathrm{h}}/\varepsilon_{\mathrm{p}}$, experiment and simulation results are compared with effective medium theory models.

matically. Fig. 1(c) elucidates the electric field distribution and space charge density of a body-centered cubic unit cell at 1 kHz, 100 kHz and 1 MHz, respectively. It shows that owing to the rise of interfacial polarization, the intensification of the electric field and space charge density on the interfaces is significant at lower frequencies. To further reveal the underlying mechanism of interfacial polarization, the corresponding low-frequency permittivity ε_{l}, characteristic frequency f_{c} and high-frequency permittivity ε_{h} obtained from FEA simulation are compared with experimental and theoretical modelling predictions, as shown in Fig. 2.

3.2. Effects of porosity and mechanical compression. To study the effect of the packing porosity on effective permittivity variations induced by interfacial polarization, we summarize the results of three different unit cells in Fig. 2(a) and (b). Predictions based on two theoretical models: Wagner's theory and Hanai' s model, corresponding to Eqs. (1) and (2), respectively, are also plotted. It is shown that, in general, the low-frequency permittivity ε_{l} decreases as the packing becomes denser (lower porosity φ) among theoretical modelling, unit cell simulation and experiments observation, indicating a strong porosity effect on effective permittivity variation due to interfacial polarization. Discrepancies exist between the theoretical modelling and experimental results, which can be attributed to the assumption in the theory where the electrical interactions between neighbouring particles was neglected. Hanai's model assumes that the mixture remains in a dilute condition after adding each infinitesimal grain in the previous step [15].

Consequently, the added infinitesimal grain at each iterative step does not exert any electrical influence on the existing grains in the mixture [24]. This assumption can be violated as the packing becomes denser (lower porosity), where the particles move closer, and electrical interactions between particles become more vigorous, leading to large deviations. As for the f_{c} variations shown in Fig. 2(b), the trend obtained by the Wagner equation contradicted that of Hanai's model, experimental and numerical observations, indicating its unsuitability for concentrated porosity ($\varphi < 0.5$). It is worth mentioning that the compression-induced porosity change shows substantial effects on both ε_{l} and f_{c} in all three experiment groups with different initial porosities. The phenomenon can also be observed in Fig. 1(b) as external compression has a significant impact on low-frequency plateau ε_{l} of effective permittivity, indicating a less pronounced manifestation of interfacial polarization as the sample undergoes compaction. Consequently, a noticeable right shift in the characteristic frequency is observed with increasing compression.

Simulations were employed to investigate the dielectric spectra of current unit cells subjected to compressive stress, similar to the experiment, to examine the effect of mechanical compression on the effective permittivity variation induced by interfacial polarization. The results reveal that mechanical compression has only a minor impact on the interfacial polarization of regularly packed samples. The obtained ε_{l} and f_{c} are compared with the experimental observations for packings with different initial porosities shown in Fig. 2(d) and (e), which states that compression stress has less pronounced effects on both ε_{l} and f_{c} for

unit cells than random packing used in the experiment within the applied stress range (below 1 MPa). This can be attributed to the structural stability of unit cells made of crystal structures under volumetric compression, maintaining their ordered packing configuration throughout the compression process. Under high compressive stress, mechanically stable packings (unit cells) experience minimal to no particle rearrangements [65,66]. Additionally, both changes in porosity and the contact region microstructure deformation for unit cells during the compression process are relatively small, thereby having a limited impact on ε_1 and f_c. However, for random packing used in experiments, the variation of ε_1 and f_c against the compressive stress are substantial, which can be attributed to the particle rearrangement as compressive stress increases, a phenomenon absents in unit cells. As external compression increases, the glass particles tend to rearrange themselves to accommodate the increased pressure [16,67,68], involving a shift in particle positions to reduce the pore space. This is supported by the comparison of porosity changes between regular packed unit cells and the experiment sample in Fig. 2(a), where a similar compressive stress is applied. The observed variations in the low-frequency effective permittivity ε_1 and characteristic frequency f_c indicates that the effects of particle arrangements in terms of porosity and particle connectivity outweigh microstructure deformation when assessing interfacial polarization effects on effective permittivity variations in water-saturated randomly packed spherical samples. Additionally, there existed a subnetwork of force chain for the sample under test in the experiment that carry a significant portion of applied external stress [21,69], where the particle-particle contacts in the force chain contain a concentrated stress. As external compression increases, the contact area between particles on the major force chain tends to increase, forming a more compact structure and facilitating the flow of free charges within the solid phase [28,55,70]. Though enhancing the conductivity, the more compact structure may reduce the interface charge accumulations, thus mitigating the effects of interfacial polarization on the effective permittivity. In our experimental range of compressive stress, the increases in contact area are constrained, implying that the improvement in solid contact conductivity might be marginal. Nevertheless, the specific area could undergo more significant changes, as the particles are inclined to reposition themselves in response to external compression. This rearrangement facilitates an increased interface area for free charges to reside between the solid and the pore fluid.

The high-frequency effective permittivity ε_h corresponds to the plateau observed at frequencies above 1 MHz in a dielectric spectrum, as shown in the experimental measurements in Fig. 1(b). This plateau primarily arises from material dipolar polarization, where the interfacial polarization due to electrical properties mismatch is absent. Comparisons of normalized high-frequency effective permittivity $\varepsilon_h/\varepsilon_s$ between the numerically simulated unit cells and two theoretical models: Maxwell-Wagner model and Hanai's DEMT model are presented in Fig. 2(c). It is apparent the simulated and experimentally observed $\varepsilon_h/\varepsilon_s$ fall within the bounds defined by those two models, with a relatively small difference compared with the predictions of the effective medium theories. The porosity of the sample demonstrates the dominating effect on the $\varepsilon_h/\varepsilon_s$, suggesting that high-frequency permittivity decreases with porosity for a given composition. The comparisons of normalized high-frequency effective permittivity $\varepsilon_h/\varepsilon_s$ between simulations and experiments subjected to comparable compressive stress are presented in Fig. 2(f). Notably, mechanical compression exhibits a negligible impact on $\varepsilon_h/\varepsilon_s$. The variations observed during the compression primarily stem from the deformation of solid particles and pore space due to particle-particle contacts, even though contact region deformations under the current stress level are relatively small.

3.3. Effects of electrical property contrasts. Simulation results and theoretical predictions for low-frequency permittivity ε_1, characteristic frequency f_c and normalized high-frequency permittivity $\varepsilon_h/\varepsilon_s$ under the effect of electrical conductivity contrast σ_s/σ_p and permittivity contrast $\varepsilon_s/\varepsilon_p$ between grains and pore phases are shown in Fig. 2(g)-(l). Gen-

erally, theoretical models exhibit similar trends for ε_1, f_c and $\varepsilon_h/\varepsilon_s$ compared to numerical simulations, though discrepancies emerge with significant two-phase electrical property contrasts. It is apparent that σ_s/σ_p significantly influences low frequency plateau, demonstrating a 10^3 fold increase in ε_1 as σ_s/σ_p increases from 1 to 10^5 as shown in Fig. 2(g). The enlargement in ε_1 indicates that more charges accumulated on the solid-liquid interfaces due to interfacial polarization, which requires more time to react and redistribute to external electrical field variations, leading to a substantial decrease in f_c. Notably, both ε_1 and f_c discrepancies between simulation results and theoretical modelling increase with higher σ_s/σ_p, emphasizing the importance of considering stronger interparticle electrical interactions for high conductivity contrast systems. However, the conductivity contrast shows no effects on normalized high-frequency permittivity $\varepsilon_h/\varepsilon_s$ in Fig. 2(i). This is because the dielectric behaviour dominates under high frequency, and the conduction loss is neglectable [70–72].

The effect of permittivity contrast ratio $\varepsilon_s/\varepsilon_p$ on effective permittivity variations is shown in Fig. 2(i) and (j). It is clear that both low-frequency permittivity ε_1 and normalized high-frequency permittivity $\varepsilon_h/\varepsilon_s$ increase with decreasing the value of $\varepsilon_s/\varepsilon_p$ ($0 < \varepsilon_s/\varepsilon_p < 1$). The increase of ε_1 indicates a more significant charge accumulation on the interfaces, which is promoted by the difference in polarization levels between the two phases. The greater the permittivity contrast, the stronger the interfacial polarization effect, and hence a more significant impact on the effective permittivity. These observations show the rate of charge transfer (controlled by σ_s/σ_p) and the ability to store charges (controlled by $\varepsilon_s/\varepsilon_p$) collectively determine the effective permittivity variation due to interfacial polarization. Moreover, this also sheds light on designing potential metamaterials with gigantic permittivity using interfacial polarization, which is likely to manifest in the presence of conductivity and permittivity contrasts between grain and pore phases [73].

3.4. Metamodel training and prediction. As discussed previously, it is evident that effective permittivity due to interfacial polarization is under the combination of effects from porosity, external compression, and electrical property contrasts. Given the limitations in theoretical modelling for low porosity grain-contacted samples and the intricacies of finite element simulation, it is challenging to accurately predict the low-frequency permittivity ε_1, characteristic frequency f_c and high-frequency effective permittivity ε_h considering the aforementioned factors. Therefore, employing ANN metamodel offers a promising guideline for predicting ε_1, f_c and ε_h once trained by the above features properly.

The objective of training the ANN model is to identify the optimal combination of hyperparameters that minimizes the MSE cost function. Therefore, scaling transformations are crucial for effective model performance, as training algorithms struggle when input features exhibit significant scale differences [58]. For example, the input conductivity contrast ranges from 1 to 10^5, while the porosity ranges from 0.24 to 0.48, then the cost function is elongated in the conductivity contrast domain, which is hard for MSE to converge. Therefore, logarithm transformations are applied to conductivity and permittivity contrasts to minimize the data range. In addition, pseudo-log transformation is used for normalized compression to account for the zero stress, where a small positive offset (10^{-5}) is added. Consequently, min-max scaling feature normalizations are conducted for all input features, rescaling the values between −1 and 1 since the hyperbolic tangent activation function expected input values from −1 to 1.

Eight different values of conductivity (σ_s/σ_p) and five permittivity contrast ($\varepsilon_s/\varepsilon_p$) are applied to all deformed cases to generate the training data with different combinations of conductivity and permittivity contrasts, porosities and compression. In total, 720 different datasets are calculated. Then, the standard correlation coefficients between every pair of attributes are calculated to better understand the correlation between input features and target output. However, it is worth noting that current ANN models are trained particularly to conclude the effects of conductivity and permittivity contrast, porosity, and compressive stress. Any new added feature to the training set requires to combine all exist-
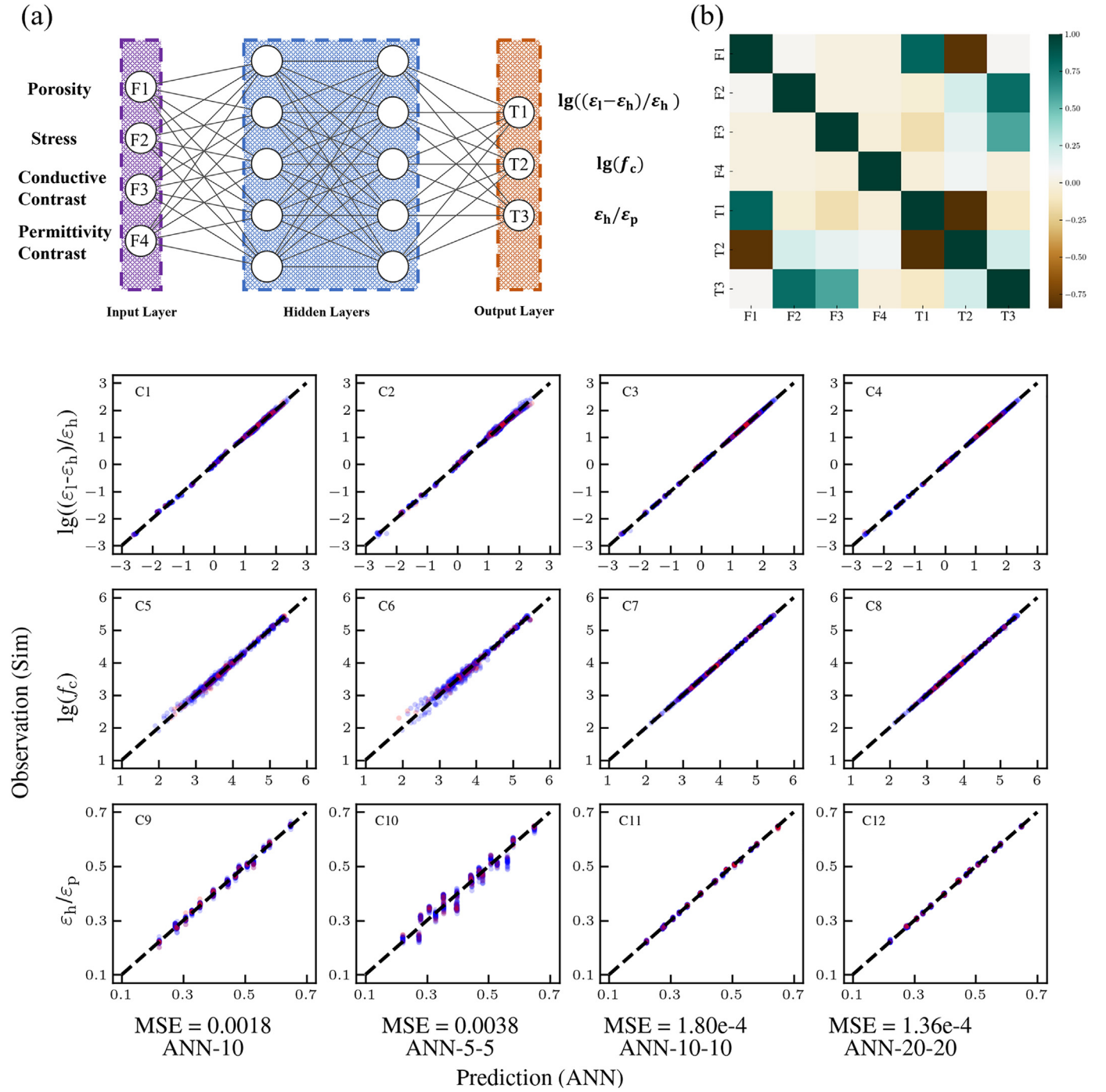
Fig. 3. (a) Schematic of an ANN consisting of two hidden with four input features (F) and three targets (T). (b) Cross-correlation coefficients between each pair of input and output features. F1 to F4 represent the conductivity contrast, permittivity contrast, porosity, and volumetric stress. T1 to T3 represent the target outputs as $\lg[(\varepsilon_l - \varepsilon_h)/\varepsilon_h]$, $\lg(f_c)$ and $\varepsilon_h/\varepsilon_p$. (c) ANN predictions on all three outputs from (I) one hidden layer with 10 neurons, (II-IV) two hidden layers with 5, 10 and 20 neurons each layer. The blue and red circular scatters represent the training and testing data, respectively. The black dashed line indicates that the predictions are equal to observations.

ing training features. For example, if grain sphericity is considered, and five aspect ratio values are selected, then the training data will be expanded 10-fold, which will require extensive computational efforts. The calculated correlation coefficients vary from −1 (strong negative correlation) to 1 (strong positive correlation), which are shown in Fig. 3(b). Seven attributes are used in the coefficient study, where conductivity and permittivity contrast, porosity and normalized stress (F1-F4) are features and $\lg[(\varepsilon_l - \varepsilon_h)/\varepsilon_h]$, $\lg(f_c)$ and $\varepsilon_h/\varepsilon_p$ (T1-T3) are the target values. The values in the upper-left to lower-right diagonal represent the at-tributes themselves and, therefore, have positive values of 1. In Fig. 3(b), it is observed that conductivity contrast (F1) shows strong correlations on T1 and T2, where the coefficients are higher than 0.5, which agrees with the observations shown in Fig. 2. Furthermore, the porosity (F3) and permittivity (F2) contrast show a relatively strong correlation (0.7) with T3. However, the correlation coefficients between input features remain low (less than 0.25). Therefore, all datasets are randomly divided into training validation and test datasets with portions of 80%, 10%, and 10%, respectively, then, feed to the ANN models.
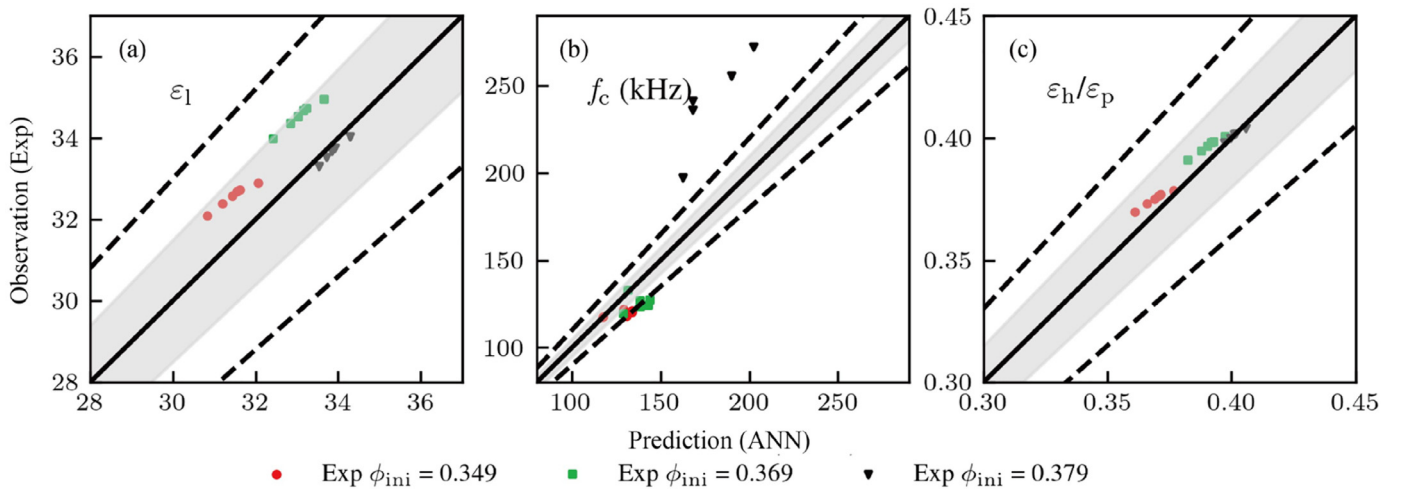
Fig. 4. Comparison between experimental observations (markers with different colours stands for different initial porosity) and metamodel (ANN-20–20) prediction on ε_l, f_c and ε_h. The black solid and dashed represent the perfect predictions and 10% error, respectively, while he respective grey shade region represents a 5% error in ANN prediction.

Four different ANN models are trained to predict the three target values. The first ANN model has only one hidden layer with 10 neurons, while the rest has two hidden layers with 5 (schematically shown in Fig. 3(a), 10, and 20 neurons in each layer, respectively. Bayesian regularization training method is used to prevent overfitting. The predicted target value $\lg(f_c)$ from four ANN models are shown in Fig. 3(c). The prediction results from ANN-5–5 have a MSE of 0.0038, which is significantly worse than the other denser models. It can also be observed that the performances of the other two hidden layer ANN models are better than the one-layer ANN-10 model ($MSE = 0.0018$). The MSEs for ANN-10–10 and ANN-20–20 are 1.80e-4 and 1.30e-4, respectively. Therefore, it is convincible that the ANN model of two hidden layers with 20 neurons each gives the best permittivity variation prediction performance with negligible MSE values.

In Fig. 3(c), we present the metamodel selections, which are based solely on results generated from numerical simulations for both training and validation. Once the chosen ANN-20–20 metamodel is adequately trained, it is applied to predict experimental observations, which differ from the simulations due to the random packing arrangement of the samples instead of the uniform unit cell lattices used in the training. The comparisons illustrated in Fig. 4(a)-(c) comparisons demonstrate that the ANN-20–20 metamodel not only captures the correct trend of effective permittivity variation caused by interfacial polarization under increasing compressive stress but also yields satisfactory predictions of low-frequency and high-frequency plateaus with an error of less than 5%. Although the trend of characteristic frequency f_c can be predicted by selected ANN metamodel correctly, the obtained values are not as accurate as other two features, which can be attribute to its sensitivity to the electrical conductivity contrast in the experiments that can be easily disturbed by the impurities in the pore fluid [22].

It is important to highlight the predictability of the present metamodel, which has been trained using solely the numerical results of simplified unit cells. The predictions were compared quantitatively with the independent experimental dataset, with only essential material and state variables. We attribute the observed discrepancies between the ANN predictions and the experimental observations to the inherent heterogeneity nature of the random packings, which differs from idealized unit cell lattices considered in simulations and training data. The unit cell models focus on the deformation due to the compression and cover the range of porosity by changing the lattice structures. The heterogeneity in granular packing can be considered with the discrete element method, where the ANN metamodel demonstrates a broader potential for providing equivalent circuit models for interparticle impedance responses [20,70,74].

Moreover, the current study focuses on the saturated state of granular media, for partially saturated states, similar approaches can be extended for the coexistence of more than one pore fluid phase. The key challenge remains the complex distributions of wetting fluids in the pore space (e.g., in the unit cells), where coalescence and hysteresis of the wetting phase are present [75].

4. Conclusion. This study investigates the effective permittivity of saturated granular materials under compression for the frequency range dominated by interfacial polarization. In the experiments, the effective permittivity spectra measured under various compressive stresses consistently exhibit a plateau-to-plateau drop, characterized by the low-frequency permittivity characteristic frequency, and high-frequency permittivity. Current study reveals that packing configuration, stress state, and contrasts of electrical properties between solid and pore fluid all contribute to the effective permittivity. We have shown that the effects of external compression induced particle rearrangement and porosity change outweigh the interparticle contact deformation in determining the effective permittivity variations due to interfacial polarization.

To integrate the effects of all these material and state parameters, we establish the multi-layer ANN metamodel trained based on a series of simulations with various unit cells, stress levels, and electrical properties. The developed ANN metamodel is capable of accurately predicting the experimental measurements within a 5% error margin for both low-frequency and high-frequency permittivity plateaus, offering a promising pathway for forecasting the dielectric behaviour of heterogeneous and multiphase materials. For further considering the realistic heterogeneity and its evolution in granular packing, the present development of metamodel can benefit particle-scale modelling and explore the interplay between the granular rearrangement and deformation.

Declaration of interests

The authors declare that they have no known competing financial interests or personal relationships that could have appeared to influence the work reported in this paper.

CRediT authorship contribution statement

Xu Wang: Conceptualization, Data curation, Formal analysis, Investigation, Methodology, Software, Validation, Visualization, Writing – original draft. **Chongpu Zhai:** Conceptualization, Funding acquisition, Investigation, Project administration, Resources, Supervision, Writing – review & editing. **Yixiang Gan:** Conceptualization, Formal analysis,

References

[1] L. Hu, et al., Interface charge characteristics in polymer dielectric contacts: analysis of acoustic approach and probe microscopy, Adv. Mater. Interfaces. (2023).

[2] A. Binley, L. Slater, Resistivity and induced polarization: theory and applications to the near-surface Earth, Cambridge University Press, 2020.

[3] Y. Jin, et al., Mechanistic model of multi-frequency complex conductivity of porous media containing water-wet nonconductive and conductive particles at various water saturations, Adv. Water. Resour. 130 (2019) 244–257.

[4] X. Zhang, et al., Superior energy storage performances of polymer nanocomposites via modification of filler/polymer interfaces, Adv. Mater. Interfaces. 5 (11) (2018) 1800096.

[5] M. Feng, et al., Recent advances in multilayer-structure dielectrics for energy storage application, Adv. Sci. 8 (23) (2021) 2102221.

[6] J.K. Yuan, et al., Giant dielectric permittivity nanocomposites: realizing true potential of pristine carbon nanotubes in Polyvinylidene fluoride matrix through an enhanced interfacial interaction, J. Phys. Chem. C 115 (13) (2011) 5515–5521.

[7] H. Luo, et al., Interface design for high energy density polymer nanocomposites, Chem. Soc. Rev. 48 (16) (2019) 4424–4465.

[8] A. Zhbanov, S. Yang, Electrochemical impedance characterization of blood cell suspensions. part 1: basic theory and application to two-phase systems, IEEE Transact. Biomed. Eng. 67 (10) (2020) 2965–2978.

[9] A.D.B. Manjunath, et al., Investigation into variation of resistivity and permittivity of aqueous solutions and soils with frequency and current density, IEEe Trans. Electromagn. Compat. 64 (2) (2022) 443–455.

[10] S. Misra, et al., Interfacial polarization of disseminated conductive minerals in absence of redox-active species—Part 2: effective electrical conductivity and dielectric permittivityInterfacial polarization due to inclusions, Geophysics 81 (2) (2016) E159–E176.

[11] Q. Niu, C. Zhang, M. Prasad, A framework for pore-scale simulation of effective electrical conductivity and permittivity of porous media in the frequency range from 1 mHz to 1GHz, Solid Earth (10) (2020) 125.

[12] J.C. Maxwell, Electricity and magnetism, 2, Dover, New York, 1954.

[13] L. Van Beek, Dielectric behaviour of heterogeneous systems, Progress Dielectr. 7 (71) (1967) 113.

[14] T. Hanai, Theory of the dielectric dispersion due to the interfacial polarization and its application to emulsions, Kolloid-Zeitschrift 171 (1) (1960) 23–31.

[15] K. Asami, Characterization of heterogeneous systems by dielectric spectroscopy, Prog. Polym. Sci. 27 (8) (2002) 1617–1659.

[16] Y. Gan, M. Kamlah, Discrete element modelling of pebble beds: with application to uniaxial compression tests of ceramic breeder pebble beds, J. Mech. Phys. Solids. 58 (2) (2010) 129–144.

[17] J. Reimann, et al., X-ray tomography investigations of mono-sized sphere packing structures in cylindrical containers, Powder. Technol. 318 (2017) 471–483.

[18] J.P. de Bono, G.R. McDowell, Investigating the effects of particle shape on normal compression and overconsolidation using DEM, Granul. Matter. 18 (3) (2016).

[19] N. Brodu, J.A. Dijksman, R.P. Behringer, Spanning the scales of granular materials through microscopic force imaging, Nat. Commun. 6 (2015) 6361.

[20] O. Birkholz, et al., Statistical investigation of structural and transport properties of densely-packed assemblies of overlapping spheres using the resistor network method, Powder. Technol. (2020).

[21] D.S. Bassett, et al., Extraction of force-chain network architecture in granular materials using community detection, Soft. Matter. 11 (14) (2015) 2731–2744.

[22] P. Leroy, et al., Complex conductivity of water-saturated packs of glass beads, J. Colloid. Interface Sci. 321 (1) (2008) 103–117.

[23] X. Chen, et al., Interfacial polarization and its influence on effective complex permittivity of mixtures, in: In 2008 International symposium on electrical insulating materials, IEEE, 2008, pp. 238–241. (ISEIM 2008).

[24] H. Chen, Q. Niu, Effects of material texture and packing density on the interfacial polarization of granular soils, Geophysics 86 (6) (2021) MR285–MR297.

[25] L. Fu, P.B. Macedo, L. Resca, Analytic approach to the interfacial polarization of heterogeneous systems, Phys. Rev. B 47 (20) (1993) 13818–13829.

[26] K.W. Wagner, Erklärung der dielektrischen Nachwirkungsvorgänge auf Grund Maxwellscher Vorstellungen, Archiv für Elektrotechnik 2 (9) (1914) 371–387.

[27] D.A. Robinson, S.P. Friedman, Electrical conductivity and dielectric permittivity of sphere packings: measurements and modelling of cubic lattices, randomly packed monosize spheres and multi-size mixtures, Physica A 358 (2–4) (2005) 447–465.

[28] D.A. Robinson, S.P. Friedman, A method for measuring the solid particle permittivity or electrical conductivity of rocks, sediments, and granular materials, Solid Earth 108 (B2) (2003).

[29] I. Krakovský, V. Myroshnychenko, Modeling dielectric properties of composites by finite-element method, J. Appl. Phys. 92 (11) (2002) 6743–6748.

[30] G.C. Topp, J.L. Davis, A.P. Annan, Electromagnetic determination of soil water content: measurements in coaxial transmission lines, Water. Resour. Res. 16 (3) (1980) 574–582.

[31] J.B. Ajo-Franklin, J.T. Geller, J.M. Harris, The dielectric properties of granular media saturated with DNAPL/water mixtures, Geophys. Res. Lett. 31 (17) (2004) n/a-n/a.

[32] D.A. Robinson, et al., A physically derived water content/permittivity calibration model for coarse-textured, layered soils, Soil Sci. Soc. America J. 69 (5) (2005) 1372–1378.

[33] Y. Chen, D. Or, Effects of Maxwell-Wagner polarization on soil complex dielectric permittivity under variable temperature and electrical conductivity, Water. Resour. Res. (6) (2006) 42.

[34] Garnett, J. Maxwell, Colours in metal glasses, in metallic films, and in metallic solutions, II. Philosoph. Transact. Royal Soc. London Ser. A 205 (1906) 237–288.

[35] D.A.G. Bruggeman, Berechnung verschiedener physikalischer Konstanten von heterogenen Substanzen. I. Dielektrizitätskonstanten und Leitfähigkeiten der Mischkörper aus isotropen Substanzen, Ann. Phys. 416 (7) (1935) 636–664.

[36] Z. Hashin, S. Shtrikman, A variational approach to the theory of the effective magnetic permeability of multiphase materials, J. Appl. Phys. 33 (10) (1962) 3125–3131.

[37] P. Sen, C. Scala, M. Cohen, A self-similar model for sedimentary rocks with application to the dielectric constant of fused glass beads, Geophysics 46 (5) (1981) 781–795.

[38] K.S. Mendelson, M.H. Cohen, The effect of grain anisotropy on the electrical properties of sedimentary rocks, Geophysics 47 (2) (1982) 257–263.

[39] S.P. Friedman, D.A. Robinson, Particle shape characterization using angle of repose measurements for predicting the effective permittivity and electrical conductivity of saturated granular media, Water. Resour. Res. 38 (11) (2002) 18-1-18-11.

[40] D.A. Robinson, S.P. Friedman, Effect of particle size distribution on the effective dielectric permittivity of saturated granular media, Water. Resour. Res. 37 (1) (2001) 33–40.

[41] U.F. Kocks, C.N. Tomé, H.R. Wenk, Texture and anisotropy: preferred orientations in polycrystals and their effect on materials properties, Cambridge university press, 2000.

[42] T.E. Doyle, et al., Modeling the permittivity of two-phase media containing monodisperse spheres: effects of microstructure and multiple scattering, Phys. Rev. B 76 (5) (2007).

[43] A. Mejdoubi, C. Brosseau, Finite-element simulation of the depolarization factor of arbitrarily shaped inclusions, Phys. Rev. e Stat. Nonlin. Soft. Matter. Phys. 74 (3) (2006) 031405 Pt 1.

[44] Abdelilah Mejdoubi, C.B., Finite-difference time-domain simulation of heterostructures with inclusion of arbitrarily complex geometry. 2006.

[45] Y. Huang, L.S. Schadler, Understanding the strain-dependent dielectric behavior of carbon black reinforced natural rubber – An interfacial or bulk phenomenon? Compos. Sci. Technol. 142 (2017) 91–97.

[46] J.H. Choi, et al., Finite-element analysis for surface discharge due to interfacial polarization at the Oil-nanocomposite interface, IEEE Trans Magn 54 (3) (2018) 1–4.

[47] A. Spanoudaki, R. Pelster, Effective dielectric properties of composite materials: The dependence on the particle size distribution, Phys. Rev. B 64 (6) (2001).

[48] C. Brosseau, A. Beroual, Computational electromagnetics and the rational design of new dielectric heterostructures, Prog. Mater. Sci. 48 (5) (2003) 373–456.

[49] V. Myroshnychenko, C. Brosseau, Finite-element method for calculation of the effective permittivity of random inhomogeneous media, Phys. Rev. e Stat. Nonlin. Soft. Matter. Phys. 71 (1) (2005) 016701 Pt 2.

[50] A. Mejdoubi, C. Brosseau, Duality and similarity properties of the effective permittivity of two-dimensional heterogeneous medium with inclusion of fractal geometry, Phys. Rev. e Stat. Nonlin. Soft. Matter. Phys. 73 (3) (2006) 031405 Pt 1): p..

[51] A.J. Pickles, M.B. Steer, Effective permittivity of 3-D periodic composites with regular and irregular inclusions, IEEe Access. 1 (2013) 523–536.

[52] N. Jebbor, S. Bri, Effective permittivity of periodic composite materials: numerical modeling by the finite element method, J. Electrostat. 70 (4) (2012) 393–399.

[53] R.M.C. Mimoso, J.M.D.S.C.R. Pereira, J.C.F. Pereira, Computational method for calculating the effective permittivity of complex mixtures, J. Microwave Power Electromagn. Energy 49 (2) (2015) 85–99.

[54] M.G. Todd, F.G. Shi, Complex permittivity of composite systems: a comprehensive interphase approach, IEEE Transact. Dielectrics Electric. Insulat. 12 (3) (2005) 601–611.

[55] X. Wang, C. Zhai, Y. Gan, Stress-dependent electrical impedance behaviours at fractal rough interfaces, Surface Topogr. 9 (2) (2021).

[56] T. Mueller, A.G. Kusne, R. Ramprasad, Machine learning in materials science: recent progress and emerging applications, Rev. Computat. Chem. 29 (2016) 186–273.

[57] J.H. van der Linden, G.A. Narsilio, A. Tordesillas, Machine learning framework for analysis of transport through complex networks in porous, granular media: a focus on permeability, Phys. Rev. E 94 (2) (2016) 022904.

[58] H. Yang, et al., Machine learning and artificial neural network prediction of interfacial thermal resistance between graphene and hexagonal boron nitride, Nanoscale 10 (40) (2018) 19092–19099.

[59] W. Fei, G.A. Narsilio, M.M. Disfani, Predicting effective thermal conductivity in sands using an artificial neural network with multiscale microstructural parameters, Int. J. Heat. Mass Transf. (2021) 170.

[60] H. Xu, et al., Guiding the design of heterogeneous electrode microstructures for Li-Ion batteries: microscopic imaging, predictive modeling, and machine learning, Adv. Energy Mater. 11 (19) (2021) 2003908.

[61] W. Zhang, J. Liu, T.C. Wei, Machine learning of phase transitions in the percolation and X Y models, Phys.Rev. E 99 (3) (2019) 032142.

[62] L.F. Lima, et al., Electric impedance of aqueous KCl and NaCl solutions: salt concentration dependence on components of the equivalent electric circuit, J. Mol. Liq. 241 (2017) 530–539.

[63] F. Kremer, A. Schönhals, Broadband dielectric spectroscopy, Springer Science & Business Media, 2002.

[64] K.L. Johnson, K.L. Johnson, Contact mechanics, Cambridge university press, 1987.

[65] S. Heitkam, W. Drenckhan, J. Fröhlich, Packing spheres tightly: influence of mechanical stability on close-packed sphere structures, Phys. Rev. Lett. 108 (14) (2012) 148302.

[66] Y. Hua, et al., Study on the stability of particle packing structure based on cells, Front. Phys. 10 (2022) 872.

[67] Y. Gan, M. Kamlah, J. Reimann, Computer simulation of packing structure in pebble beds, Fus. Eng. Design 85 (10–12) (2010) 1782–1787.

[68] J. Wiącek, M. Molenda, Effect of particle size distribution on micro- and macrome-chanical response of granular packings under compression, Int. J. Solids. Struct. 51 (25–26) (2014) 4189–4195.

[69] F. Radjai, et al., Force distributions in dense two-dimensional granular systems, Phys. Rev. Lett. 77 (2) (1996) 274.

[70] C. Zhai, et al., Stress-dependent electrical transport and its universal scaling in gran-ular materials, Extreme Mech. Lett. 22 (2018) 83–88.

[71] D.P. Almond, C.R. Bowen, Anomalous power law dispersions in ac conductivity and permittivity shown to be characteristics of microstructural electrical networks, Phys. Rev. Lett. 92 (15) (2004) 157601.

[72] D.P. Almond, C.R. Bowen, D.A.S. Rees, Composite dielectrics and conductors: simu-lation, characterization and design, J. Phys. D. Appl. Phys. 39 (7) (2006) 1295–1304.

[73] J. Roscow, C. Bowen, D. Almond, Breakdown in the case for materials with giant permittivity? ACS. Energy Lett. 2 (10) (2017) 2264–2269.

[74] O. Birkholz, Y. Gan, M. Kamlah, Modeling the effective conductivity of the solid and the pore phase in granular materials using resistor networks, Powder. Technol. 351 (2019) 54–65.

[75] Z. Shi, Z. Wang, Y. Gan, Effects of topological disorder in unsaturated granular media via a pore-scale lattice Boltzmann investigation, Adv. Water. Resour. 149 (2021) 103855.